PHYSICAL REVIEW E **88**, 062915 (2013)

Clustering in delay-coupled smooth and relaxational chemical oscillators

Karen Blaha,[1] Judith Lehnert,[2] Andrew Keane,[2] Thomas Dahms,[2] Philipp Hövel,[2,3] Eckehard Schöll,[2] and John L. Hudson[1]
[1]*Department of Chemical Engineering, University of Virginia, Charlottesville, Virginia 22902, USA*
[2]*Institut für Theoretische Physik, TU Berlin, Hardenbergstraße 36, 10623 Berlin, Germany*
[3]*Bernstein Center for Computational Neuroscience, Humboldt-Universität zu Berlin, Philippstraße 13, 10115 Berlin, Germany*
(Received 17 June 2013; published 16 December 2013)

We investigate cluster synchronization in networks of nonlinear systems with time-delayed coupling. Using a generic model for a system close to the Hopf bifurcation, we predict the order of appearance of different cluster states and their corresponding common frequencies depending upon coupling delay. We may tune the delay time in order to ensure the existence and stability of a specific cluster state. We qualitatively and quantitatively confirm these results in experiments with chemical oscillators. The experiments also exhibit strongly nonlinear relaxation oscillations as we increase the voltage, i.e., go further away from the Hopf bifurcation. In this regime, we find secondary cluster states with delay-dependent phase lags. These cluster states appear in addition to primary states with delay-independent phase lags observed near the Hopf bifurcation. Extending the theory on Hopf normal-form oscillators, we are able to account for realistic interaction functions, yielding good agreement with experimental findings.

DOI: 10.1103/PhysRevE.88.062915 PACS number(s): 05.45.Xt, 02.30.Ks, 05.45.Gg, 82.40.Qt

I. INTRODUCTION

The field of nonlinear dynamics in coupled systems has seen a huge increase in interest in recent years [1–5]. The systems range from a few coupled elements to complex networks. Collective dynamics may arise in various patterns, of which in-phase (or zero-lag) synchronization is the most prominent. Traveling waves [6,7] and cluster or group synchronization [8–10] are other examples. In particular, during cluster synchronization, parts of a network synchronize with zero lag, but with a nonzero phase-lag between different clusters. Interest in cluster synchrony has led to significant theoretical [8–13] and experimental [14–18] results.

A recent theoretical study [19] discussed cluster synchronization in delay-coupled networks of Hopf normal-form oscillators (also known as Stuart-Landau oscillators), which are given by a generic model of a Hopf bifurcation. Depending upon the delay time, different cluster states exist and are stable. These intervals overlap leading to multistable regimes; i.e., the specific state that is realized is determined by the initial conditions. In Ref. [19] it was shown that the phase of a complex coupling constant can be used to select a desired cluster state.

Combining theoretical analysis with experiments, chemical oscillators can be mathematically described by very simple models like the Kuramoto phase oscillator model or the Stuart-Landau model in certain regimes of operation. In the present paper, we study a system of four chemical oscillators coupled in a unidirectional ring.

We consider two regimes of operation: (1) For low-bias voltages, the elements show smooth sinusoidal oscillations and we are able to verify the results of Ref. [19] experimentally. The theory not only correctly predicts the interval where each cluster state exists but also quantitatively the common frequency that arises depending upon the delay time and the particular cluster state. We show that the time delay can be used to ensure the existence and stability of a desired cluster state, instead of the phase of a complex coupling constant, which is unavailable in the experiment. (2) For a higher bias voltage, the oscillations become of the strongly nonlinear relaxational type. In this regime, cluster synchronization with secondary cluster states, i.e., unequal phase differences between the clusters, can occur in addition to symmetric cluster states. We introduce an extended version of the Stuart-Landau model, based on experimentally measured interaction functions. Linear stability analysis and numerical continuation allow for a theoretical treatment of these states.

This paper is organized as follows: In Sec. II we present a short summary of relevant results from Ref. [19]. We introduce the theoretical model and carry out the analysis that allows us to predict intervals of existence and common frequencies of the different cluster states. The experiment using chemical oscillators is described in detail in Sec. III. Section IV deals with the corresponding experimental results for the smooth oscillators. Having identified limitations in the existing theory, we adapt the theoretical model for more general use and apply it again to the chemical oscillators in the relaxational regime using a higher bias voltage in Secs. V and VI. Details of the extended theory are given in Sec. VI A. Finally, we conclude with Sec. VII.

II. THEORETICAL MODEL: SINUSOIDAL OSCILLATIONS

In this section we give a short summary of the results obtained in Ref. [19], where cluster synchronization and stability in a network of N Stuart-Landau oscillators were investigated. We focus on the case that is relevant to the considered experimental setup (see Sec. III), namely a topology given by a unidirectionally coupled ring and the case of real coupling constant. In Refs. [19] and [20] more general topologies and complex coupling constant were discussed as well.

The dynamics of the Stuart-Landau oscillators in a unidirectionally coupled ring is given by

$$\dot{z}_j = f(z_j) + K z_{(j+1) \bmod N}(t-\tau), \tag{1}$$

with $z_j = r_j e^{i\varphi_j} \in \mathbb{C}$, $j = 1,\ldots,N$, time delay τ, and coupling strength K. For notational convenience, we will drop the modulus N in the indices in the following, i.e., $z_{j+1} \equiv z_{(j+1) \bmod N}$. Note that in Ref. [19] a diffusion-like coupling was used. There, the coupling term reads $z_{j+1}(t-\tau) - z_j$ instead of just $z_{j+1}(t-\tau)$. Nevertheless, this alters the involved equations only slightly so that we only have to adapt the analysis of Ref. [19] at a few points.

The local dynamics of each element is given by the normal form of a supercritical Hopf bifurcation:

$$f(z) = [\lambda + i\omega - (1 + i\gamma)|z|^2]z, \tag{2}$$

with real constants $\lambda, \omega \neq 0$, and γ. This class of systems arises naturally as a generic expansion in center manifold coordinates near a Hopf bifurcation, and therefore its dynamics is generic for many systems close to the Hopf bifurcation.

In polar coordinates with radius and phase variables the system Eq. (1) reads as follows:

$$\dot{r}_j = \left(\lambda - r_j^2\right) r_j + K r_{j+1}(t-\tau)\cos[\varphi_{j+1}(t-\tau) - \varphi_j(t)] \tag{3a}$$

$$\dot{\varphi}_j = \omega - \gamma r_j^2 + K\frac{r_{j+1}(t-\tau)}{r_j}\sin[\varphi_{j+1}(t-\tau) - \varphi_j(t)]. \tag{3b}$$

Cluster states with a common amplitude and equal phase lags between neighboring nodes can be described by $r_j \equiv r_{0,m}$ and $\varphi_j = \Omega_m t + j\Delta\varphi_m$ with collective frequency Ω_m and $\Delta\varphi_m = 2\pi m/N$. Such states we call *primary states*. In contrast, the nodes of *secondary states* as discussed in Sec. VI are still characterized by a common collective frequency but different amplitudes and phase lags. The integer $m = 0,\ldots,N-1$ labels the specific states: In the case of four nodes, $m = 0$ corresponds to zero-lag synchronization, $m = 1$ is the splay state, $m = 2$ the two-cluster state, while $m = 3$ labels the reverse splay state (see below). Applying this notion to Eqs. (3) yields the following set of transcendental equations for the collective amplitude $r_{0,m}$ and frequency Ω_m of the m-state:

$$r_{0,m}^2 = (\lambda + K\cos\Phi_m) \tag{4a}$$

$$\Omega_m = \omega - \gamma r_{0,m}^2 + K\sin\Phi_m, \tag{4b}$$

where $\Phi_m = \Delta\varphi_m - \Omega_m\tau$. Note that Ω_m only depends on $r_{0,m}$ if $\gamma \neq 0$. Thus, the parameter γ couples the frequency to the oscillation amplitude (anisochronicity).

Considering small deviations δr_j and $\delta\varphi_j$, we obtain $r_j = r_{0,m}(1 + \delta r_j)$, $\varphi_j = \Omega_m t + j\Delta\varphi_m + \delta\varphi_j$, $\xi_j = (\delta r_j, \delta\varphi_j)^T$. This leads to a variational equation for the m-cluster state:

$$\dot{\xi} = \mathbf{I}_N \otimes (\mathbf{J}_{0,m} - K\mathbf{R}_m)\xi + K(\mathbf{A} \otimes \mathbf{R}_m)\xi(t-\tau), \tag{5}$$

with the $2N$-dimensional vector $\xi = (\xi_1,\ldots,\xi_N)^T$, the $N \times N$ identity matrix $\mathbf{I}_N$, and matrices $\mathbf{R}_m = \begin{pmatrix} \cos\Phi_m & -\sin\Phi_m \\ \sin\Phi_m & \cos\Phi_m \end{pmatrix}$, $\mathbf{J}_{0,m} = \begin{pmatrix} -2r_{0,m}^2 & 0 \\ -2\gamma r_{0,m}^2 & 0 \end{pmatrix}$. The adjacency matrix $\mathbf{A}$ describes the unidirectional ring topology: $a_{ij} = 1$ for $j = i+1$ and zero otherwise. Diagonalizing $\mathbf{A}$, we arrive at the block-diagonalized variational equation

$$\dot{\zeta}_k(t) = \mathbf{J}_{0,m}\zeta_k(t) - K\mathbf{R}_m[\zeta_k(t) - \nu_k\zeta_k(t-\tau)], \tag{6}$$

where $\nu_k = e^{2ik\pi/N}$, $k = 0,1,\ldots,N-1$, are the eigenvalues of $\mathbf{A}$. Note that Eq. (6) can be considered as a master stability equation [21] for Eq. (1). Here, the coefficient matrices $\mathbf{J}_{0,m}$ and $\mathbf{R}_m$ do not depend on time. Hence, the Floquet exponents of the synchronized periodic state are given by the eigenvalues Λ of the characteristic equation

$$\det\{\mathbf{J}_{0,m} - \Lambda\mathbf{I}_2 + K(-1 + e^{2ik\pi/N - \Lambda\tau})\mathbf{R}_m\} = 0. \tag{7}$$

If for all $k = 0,\ldots,N-1$ all Floquet exponents (except the one relating to the Goldstone mode) have a negative real part, the cluster state with index m will be stable.

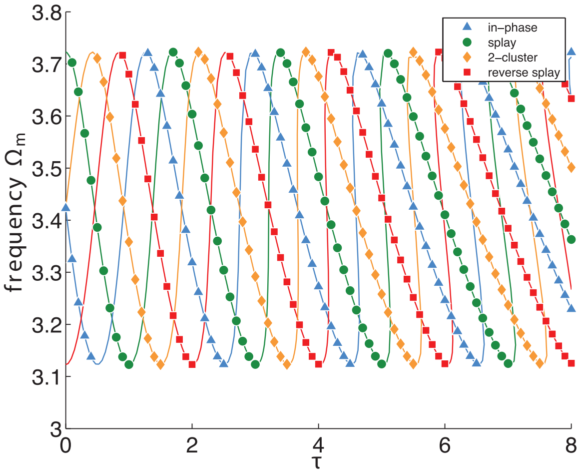

FIG. 1. (Color online) Collective frequency Ω_m versus the time delay τ obtained as numerical solutions of Eqs. (4). Stable solutions: Gray (blue) triangles: in-phase state. Black (green) circles: splay state. Gray (orange) diamonds: two-cluster state. Black (red) squares: reverse splay state. Blank curves refer to unstable solutions. The stability is determined via Eq. (7). Parameters: $\lambda = 1.1025$, $\omega = 3.4228$, $\gamma = 0$, $K = 0.3$, $N = 4$.

Figure 1 depicts the common frequencies of all four possible states in a unidirectionally coupled ring of four elements. Symbols and blank curves refer to stable and unstable solutions, respectively, where the stability is calculated via the characteristic equation (7). It can be seen that for most values of τ multistability between different states exists, but that all four cluster states do not necessarily occur for every value of τ. However, it is always possible to choose the delay in such a way that the desired m-state exists with a frequency Ω_m. Using the delay time

$$\tau_{\mathrm{m}} = \frac{2\pi m}{N\Omega_m}, \tag{8}$$

Eq. (4b) holds for $\Phi_m = 0$, so that $\Omega_m = \omega - \gamma(\lambda + K)$. From $\Phi_m = 0$ we also have $\mathbf{R}_m = \mathbf{I}_2$, meaning that Eq. (7) simplifies to:

$$[-2r_{0,m} + K(-1 + e^{2ik\pi/N - \Lambda\tau}) - \Lambda] \times [K(-1 + e^{2ik\pi/N - \Lambda\tau}) - \Lambda] = 0. \tag{9}$$

The dominant Floquet exponent is always obtained by setting the second factor to zero: $\Lambda = K(-1 + e^{2ik\pi/N - \Lambda\tau})$. The solution Λ of this equation will always have a negative real part [19]. Note that the choice τ_{m} only guarantees the existence and stability of the m-state, but does not ensure monostability. In fact, for the parameter choice of Fig. 1 and generally for large enough delay times, multistability clearly persists for $\tau = \tau_m$.

III. EXPERIMENTAL SETUP

The experimental setup is described in the following. Experiments are performed in an electrochemical cell consisting of four 1-mm-diameter Ni working electrodes (99.98% pure), a Pt mesh counter electrode, and $Hg/Hg_2SO_4/K_2SO_4$ (sat) reference electrode, with a 3M H_2SO_4 electrolyte, shown in Fig. 2(a). The four electrodes are electrically coupled in a unidirectional ring. The cell is enclosed in a jacketed glass vessel maintained at a temperature of 11°C. An ACM Instruments multichannel potentiostat is used to set the potentials V_0 of the electrodes such that they undergo transpassive dissolution. A resistor, $R_p = 650\,\Omega$, is attached to each electrode, causing the dissolution currents I_j to oscillate [22]. These resulting electrodissolution currents are measured at 250 Hz using zero resistance amperemeters (ZRAs) attached to a real-time data acquisition system.

Four oscillators with similar frequencies are selected from an array of 64 oscillators. The character of the oscillators may be varied by the choice of applied voltage. Experiments are performed at two voltages: a low voltage to induce nearly harmonic oscillations, which can be modeled by Stuart-Landau oscillators (cf. Sec. IV), and a higher voltage exhibiting higher harmonics and more complex behavior (cf. Sec. VI). We will use the terms *smooth* and *relaxation* oscillations, respectively. Negligible intrinsic electrical interactions exist between the uncoupled oscillators [23]. The startup or shutdown of an oscillator does not alter the behavior of the other oscillators. Furthermore, the oscillator dynamics has no interdependence when oscillators are functioning in the uncoupled state.

Interactions are introduced using real-time coupling of the form

$$V_j(t) = V_0 + \delta V_j(t), \tag{10}$$

where δV_j are the changes in the circuit potentials of the jth elements due to the feedback. These feedback voltages are given by

$$\delta V_j(t) = K \sum_{n=1}^{N} a_{jn}[V_n(t-\tau) - R_p \hat{I}_n(t-\tau)], \tag{11}$$

where $R_p = 650\,\Omega$ is the channel resistance, K is the fixed overall coupling gain, and τ denotes the coupling time delay, which is realized by the real-time data acquisition system combined with the multichannel potentiostat. $\hat{I}_n$ are the normalized currents measured by the ZRAs.

To obtain this quantity, the measurements of the dissolution current I_n are first scaled such that the mean value of each channel $\bar{I}_n$ is removed as an offset. Then, we perform normalization of the amplitude of the oscillation $I_n^{\max}$ relative to the mean amplitude of the electrode ensemble $N^{-1}\sum_{n=1}^{N} I_n^{\max}$. a_{jn} is an element of the adjacency matrix $\mathbf{A}$, which describes the structure of the coupling. We apply unidirectional coupling on a four-member ring with the adjacency matrix

$$\mathbf{A} = \begin{pmatrix} 0 & 1 & 0 & 0 \\ 0 & 0 & 1 & 0 \\ 0 & 0 & 0 & 1 \\ 1 & 0 & 0 & 0 \end{pmatrix}. \tag{12}$$

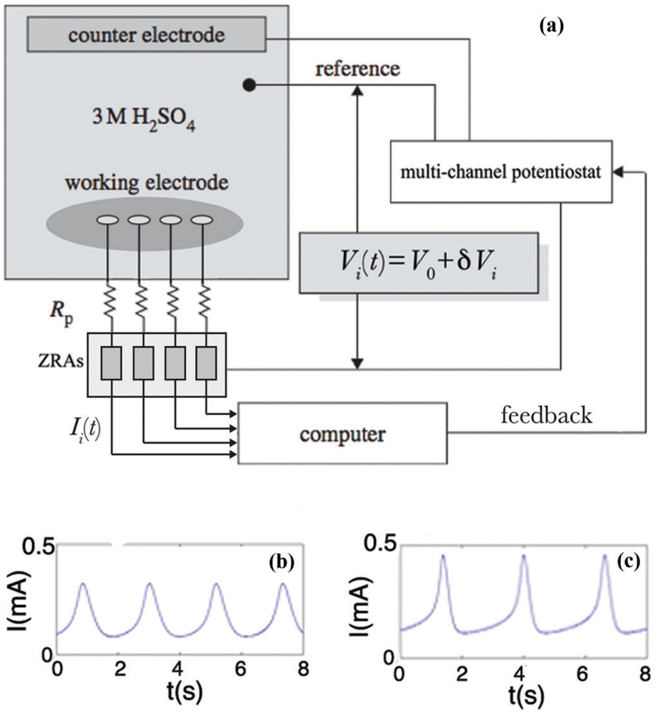

FIG. 2. (Color online) (a) Experimental apparatus with multichannel addressable feedback, R_p is the channel resistance of $650\,\Omega$. (b) Electrochemical dissolution time series showing smooth oscillators at a potential of $V_0 = 1.105$ V. (c) Time series of relaxation oscillators at $V_0 = 1.2$ V. ZRA: zero resistance amperemeter.

This coupling scheme is implemented via the multichannel potentiostat (see Fig. 2).

We calculate the dynamical variables (amplitudes r_j and phases φ_j) from the ZRAs' experimental measurement of the electrodissolution current of each oscillator (see Fig. 2). From these currents, the phase of each oscillator is found by peak-to-peak linear interpolation, where the peak is defined as 0 or 2π [24]. From the phases, we can then calculate the average frequencies of the oscillators. The amplitudes are measured as half of the difference between the peak and trough value of the electrodissolution current, giving one data point per period.

The parameters λ and ω that belong to the theoretical model can be identified by the dynamics of a single uncoupled oscillator [see Figs. 2(b) and 2(c)]. λ must be set such that the amplitude r is equal to $\sqrt{\lambda}$, while ω should be chosen such that the period of oscillation must be equal to $2\pi/\omega$. In the experiments ω is not identical for each oscillator, but the oscillators are chosen so that the values of ω are very close to each other. As such ω is simply taken to be the average (i.e., $\omega = N^{-1}\sum_{j=1}^{N} \omega_j$). Furthermore, we let γ be equal to zero, i.e., the frequency does not depend on the radius.

IV. SMOOTH OSCILLATIONS

In this section we consider the case of smooth sinusoidal oscillations. The four electrodes were held at a voltage of $V_0 = 1.105$ V. This is slightly above a Hopf bifurcation that occurs at $V_0 \approx 1.05$ V. Hence the oscillations are nearly harmonic [cf. Fig. 2(b)]. Although visually the time series is not perfectly sinusoidal, in practice we can model the oscillators' phase dynamics as linear [25].

The four oscillators operate at $\omega_1 = 3.424 \pm 0.063$ rad/s, $\omega_2 = 3.393 \pm 0.069$ rad/s, $\omega_3 = 3.418 \pm 0.063$ rad/s, and $\omega_4 = 3.456 \pm 0.057$ rad/s. The frequency range is due to the slow drift of the natural frequencies of the oscillators.

Figure 3 depicts the measured and numerically calculated, stable states of the compound system depending upon the time delay in Figs. 3(a) and 3(b), respectively. In Fig. 3(b), lines are calculated from Eqs. (4) and points are based on solution continuation of Eqs. (3) using DDE-BIFTOOL. In order to resolve the multistability present in the coupled system we slowly increase the time delay [shown by arrows in Fig. 3(a)] up to $\tau = 1.25 \times (2\pi/\omega)$ at which point we perform a down-ramping. During the up-sweep, τ is increased from $0.80 \times (2\pi/\omega)$ to $1.25 \times (2\pi/\omega)$ in increments of $0.05 \times (2\pi/\omega)$. The system is allowed to reach a stationary state at each value of τ. The qualitatively different states are marked by the following symbols: red squares represent the reverse splay state, blue triangles represent the in-phase state, and green circles represent the splay state.

We start at $\tau = 0.8 \times (2\pi/\omega)$ with a reverse splay state, which is characterized by a phase difference of $3\pi/2$ between two subsequent oscillators. Increasing to $\tau = 0.95 \times (2\pi/\omega)$, we obtain in-phase synchronization with $\varphi_1 = \varphi_2 = \varphi_3 = \varphi_4$. For larger τ values, the system exhibits a splay state; that is, the phase difference is $\pi/2$ between two subsequent oscillators.

During the down-sweep, the time delay is decremented by $0.05 \times (2\pi/\omega)$ until $\tau = 0.75 \times (2\pi/\omega)$. We observe the same states in the down-sweep as the up-sweep. Each time τ is decremented, the frequency increases slightly, except when a cluster transition occurs and the frequency abruptly jumps to a lower value. The system maintains the splay state until transitioning to the in-phase cluster state and then the reverse splay state. The transitions are also shown by arrows for the up- and down-sweep. Note that they occur at different time delays depending upon the direction of the time delay sweep. The coexistence of several cluster states at a given value of τ, which depends upon the prior state of the system, demonstrates hysteresis. In Fig. 3(a), showing the experimental data, the triangles representing the in-phase cluster state are slightly

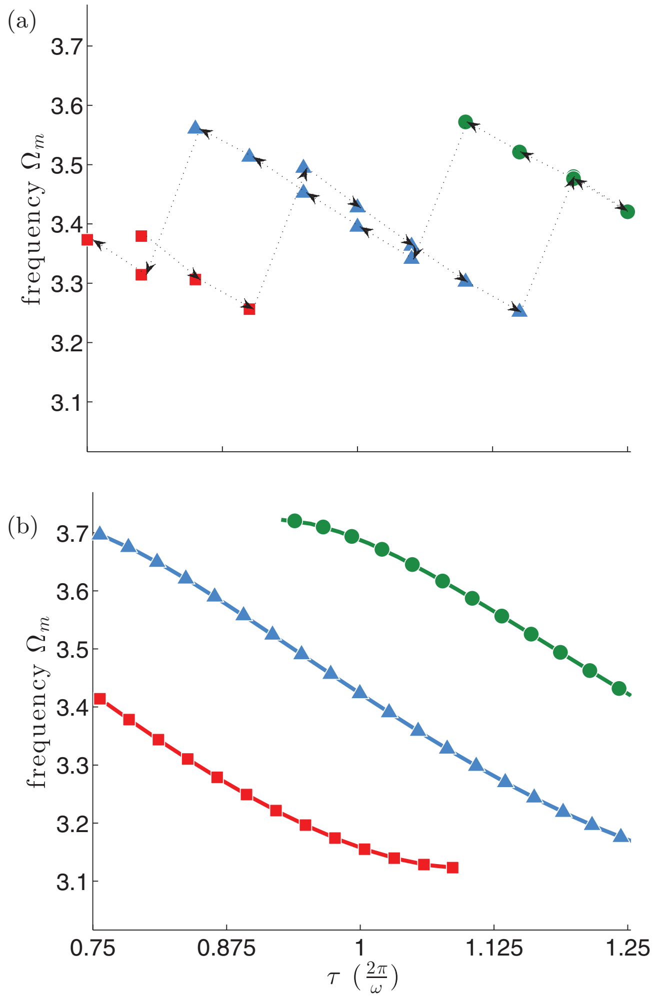

FIG. 3. (Color online) Collective frequency Ω_m versus the time delay τ. (Red) squares, (blue) triangles, and (green) circles represent a reverse splay state, an in-phase state, and a splay state, respectively. (a) Experimental data, $V_0 = 1.105$ V, $K = 0.15$. The arrows indicate an increase or decrease of τ during the measurement. (b) Solution continuation of Eqs. (3) using DDE-BIFTOOL (symbols) and numerical solutions of Eqs. (4) (lines). Parameters as in Fig. 1.

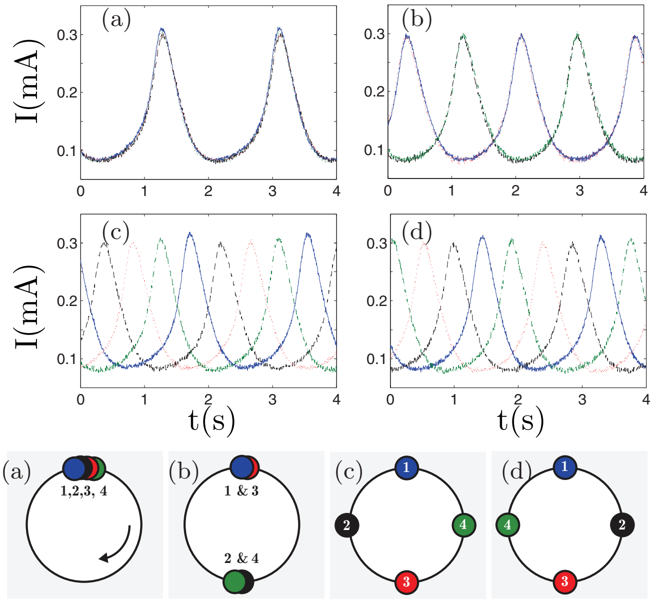

FIG. 4. (Color online) Experimental time series (top) and schematic diagram (bottom) of an in-phase state (a), a two-cluster state (b), a reverse splay state (c), and a splay state (d) as shown in Fig. 3(a). The schematics show phase relations between oscillators on the phase ring. Oscillator colors in the schematic correspond to the colors in the times series: φ_1 is shown in blue (solid), φ_2 is black (dashed), φ_3 is red (dotted), and φ_4 is green (dot-dashed). Parameters: $V_0 = 1.105$ V, $K = 0.15$; time delays: (a) $\tau = 1.05 \times 2\pi/\omega$, (b) $0.5 \times 2\pi/\omega$, (c) $1.2 \times 2\pi/\omega$, and (d) $0.8 \times 2\pi/\omega$ with $\omega = 3.4228$ rad/s as in Fig. 1, respectively.

nonidentical near $\tau = 1 \times (2\pi/\omega)$; this is due to drift in the natural frequencies during the course of the experiment.

Figures 4(a)–4(d) illustrate the qualitative differences between the cluster states seen in Fig. 3. Next to the time series, corresponding schematic diagrams are also depicted. Note that the two-cluster state [Fig. 4(b)] does not occur in the range of τ shown in Fig. 3.

We see that the cluster states and hysteresis can be modeled by the Stuart-Landau oscillator as given in Eqs. (3). The numerical results, including simulations as well as path continuation using DDE-BIFTOOL [26,27], shown in Fig. 3(b) closely match the experimental results. The only discrepancy seen is that the branches of each cluster state in the experiments seem to be stable for a shorter range of τ, leading to an earlier jump to another cluster state. This is probably due to experimental noise and small heterogeneities in the oscillators' parameters.

V. INTERACTION FUNCTIONS

If we increase the voltage to $V_0 = 1.2$ V, the profile of the oscillations deforms from a sinusoidal to a strongly nonlinear relaxation oscillation. One could use a nonlinear time transformation to map the relaxation oscillations back to the sinusoidal model and thus still employ the Stuart-Landau model for a theoretical description. However, this nonlinear time transformation will also affect the coupling, which no longer can be assumed to be sinusoidal. Instead we rewrite Eqs. (3) in a more general form:

$$\dot{r}_j = \left(\lambda - r_j^2\right) r_j + K r_{j+1}(t-\tau) H_r[\varphi_{j+1}(t-\tau) - \varphi_j(t)] \tag{13a}$$

$$\dot{\varphi}_j = \omega + K \frac{r_{j+1}(t-\tau)}{r_j} H_\varphi[\varphi_{j+1}(t-\tau) - \varphi_j(t)], \tag{13b}$$

where H_r and H_φ are coupling functions, also called interaction functions, which can be obtained experimentally.

To determine H_r and H_φ, we conduct a separate but related experiment according to the methods described in Refs. [24,28, 29]. We select two oscillators at the same voltage with slightly different natural frequencies and couple them such that they interact but do not phase lock. We measure the time-dependent radius $r_j[\varphi_i(t) - \varphi_j(t)]$ and the frequency $\Omega_j[\varphi_i(t) - \varphi_j(t)]$ of oscillator j as a function of phase difference $\Delta\varphi = \varphi_i(t) - \varphi_j(t)$. We find that r_j and $\Delta\varphi$ are approximately constant over one oscillation period. Following Ref. [28] with stationary radii r_j, we use

$$H_\varphi(\Delta\varphi) = -\frac{2\pi\,\Delta T_j}{T_j^2}\frac{1}{K}, \tag{14}$$

where ΔT_j denotes the deviation from the natural period T_j. We choose K equal to the maximum of the first factor. This yields $\max_{\Delta\varphi} H(\Delta\varphi) = 1$ as shown in Figs. 5(a) and 5(b). Setting $\dot{r}_j = 0$ in Eq. (13a), we obtain

$$H_r(\Delta\varphi) = \frac{1}{K}[r(\Delta\varphi)^2 - \lambda], \tag{15}$$

where $\sqrt{\lambda}$ is experimentally measured as the time average of r over the course of the experiment.

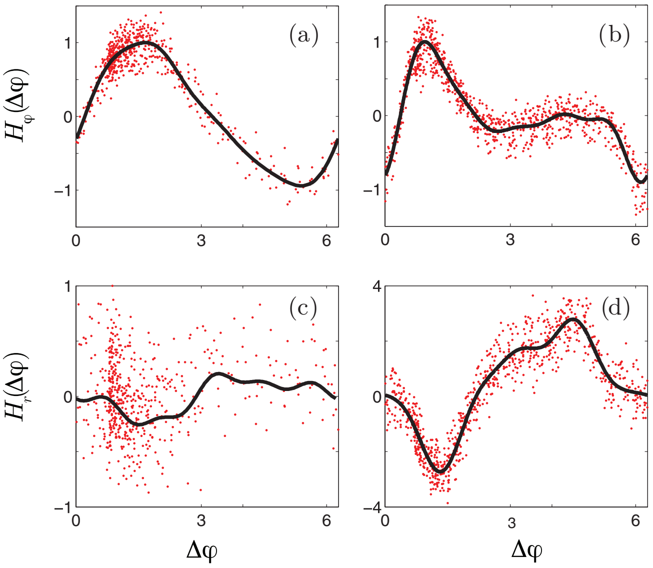

FIG. 5. (Color online) Phase interaction function H_φ in panels (a) and (b) for $V_0 = 1.105$ V and $V_0 = 1.2$ V, respectively; radial interaction function H_r in panels (c) and (d) for $V_0 = 1.105$ V and $V_0 = 1.2$ V, respectively. Experimentally obtained data is shown in gray (red) dots. A five-term Fourier fit from evenly sampled data is shown by the black curve.

Figure 5 shows the two interaction functions H_r and H_φ for the low voltage $V_0 = 1.105$ V in Figs. 5(a) and 5(c) and for the higher voltage $V_0 = 1.2$ V in Figs. 5(b) and 5(d). The (black) curve is a fifth-order Fourier fit from evenly sampled data.

For $V_0 = 1.105$ V, the radial interaction function remains approximately constant and the phase interaction function exhibits a sinusoidal shape. Thus, we have $H_\varphi(\Delta\varphi) = \sin(\Delta\varphi)$ as considered in Eqs. (3).

At this point, we also see a possible cause for the difference between Figs. 3(a) and 3(b). The numerically calculated frequencies coincide with the use of an appropriate phase interaction function. Since we have assumed $\gamma = 0$, the radial interaction function does not influence the frequencies, but it does influence the stability of the particular state. The lack of an appropriate radial interaction function might explain the difference between the stability of the states shown in Figs. 3(a) and 3(b).

For $V_0 = 1.2$ V, both interaction functions have a more complex structure. In order to take their complex shapes into account in our theory, we approximate H_r and H_φ by Fourier series up to the fifth order. How well this approach works is the topic of the following section.

VI. RELAXATION OSCILLATIONS

In this section, we present the results for operation at a higher voltage compared to Sec. IV, that is, further away from the Hopf bifurcation. We fix the voltage of the system at $V_0 = 1.2$ V, such that the electrode current oscillates in a relaxational fashion. We perform experiments similar to the one in Sec. IV with four oscillators coupled in a unidirectional ring but consider a different range for the time delay.

The oscillators for these experiments now have different intrinsic frequencies compared to Sec. IV. For the experiment yielding the results seen in Fig. 6 the four oscillators operate at

$\omega_1 = 2.421 \pm 0.068$ rad/s, $\omega_2 = 2.445 \pm 0.088$ rad/s, $\omega_3 = 2.407 \pm 0.069$ rad/s, and $\omega_4 = 2.449 \pm 0.112$ rad/s. During the experiment yielding the results seen in Fig. 8, they operate at $\omega_1 = 2.495 \pm 0.109$ rad/s, $\omega_2 = 2.510 \pm 0.124$ rad/s, $\omega_3 = 2.448 \pm 0.094$ rad/s, and $\omega_4 = 2.515 \pm 0.097$ rad/s.

For the chosen voltage, the interaction functions have a more complex shape [cf. Figs. 5(b) and 5(d)] and are approximated by fifth-order Fourier series. Therefore, we describe the experiment by the following set of delay-coupled Stuart-Landau equations:

$$\dot{r}_j = (\lambda - r_j^2)r_j + K\sum_{n=1}^{N} a_{jn} r_n(t-\tau)\left(\sum_{l=0}^{5} a_{l,r}\cos\{l[\varphi_n(t-\tau)-\varphi_j]\} + b_{l,r}\sin\{l[\varphi_n(t-\tau)-\varphi_j]\}\right), \qquad (16a)$$

$$\dot{\varphi}_j = \omega + K\sum_{n=1}^{N} a_{jn}\frac{r_n(t-\tau)}{r_n}\left(\sum_{l=0}^{5} a_{l,\varphi}\cos\{l[\varphi_n(t-\tau)-\varphi_j]\} + b_{l,\varphi}\sin\{l[\varphi_n(t-\tau)-\varphi_j]\}\right), \qquad (16b)$$

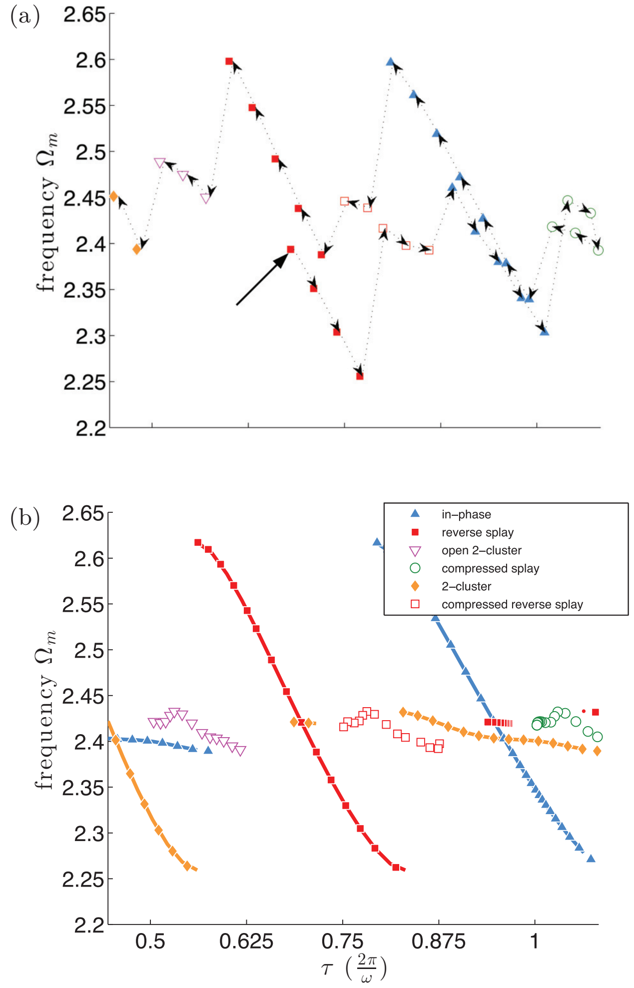

FIG. 6. (Color online) Dynamics in dependence on the time delay τ. (a) Experimental data, $V_0 = 1.2$ V, $K = 0.10$. The starting state is marked by a black arrow. The increasing and decreasing of τ during the experiment are shown with arrows. (b) Solutions of Eqs. (16) using the continuation tool DDE-BIFTOOL (markers) and numerical solutions of Eqs. (4) (lines). In-phase, two-cluster, compressed splay, reverse splay, compressed reverse splay, and open two-cluster states are represented by upward-triangles, diamonds, open circles, squares, open squares, and downward-triangles, respectively. The interaction functions H_r and H_φ are chosen as in Eqs. (16) and Table I. Parameters: $\lambda = 2.890$, $K = 0.189$, and $\omega = 2.430$.

where the Fourier coefficients $a_{l,r}, b_{l,r}, a_{l,\varphi}$, and $b_{l,\varphi}$ are determined by a fit to the experimentally obtained interaction functions H_r and H_φ. The coefficients are given in Table I. They are normalized such that $\max|H_\varphi| = 1$. The coupling strength K still represents the overall coupling strength.

The relaxation oscillators exhibit more complicated cluster and hysteresis behavior as depicted in Figs. 6(a) and 6(b) for experimental and numerical data, respectively. For the latter we use the continuation software DDE-BIFTOOL similar to the case of smooth oscillators. The detected states agree very well with the experimental results in Figs. 6(a), where the black arrow marks the starting configuration. Note that only stable solutions relevant to the experimental results are shown. For the comparison between Figs. 6(a) and 6(b), it must also be noted that while the natural frequency ω varies slowly during the experiments due to drift, it is kept constant in our numerical calculations.

We find a sequence of different cluster states as the time delay τ is increased or decreased. The primary states discussed earlier in Fig. 4 (in-phase, two-cluster, reverse splay, and splay states) are also present in the case of the relaxational oscillators. In the current regime of operation additional qualitatively different states are possible. These *secondary states* are investigated in the following.

The relaxation oscillators still demonstrate hysteresis as τ is increased and decreased. In a population of smooth

TABLE I. Fourier coefficients used in Eqs. (16).

Radial interaction function	
$a_{1,r} = -0.97948$,	$b_{1,r} = -1.82354$
$a_{2,r} = 0.36110$,	$b_{2,r} = -0.07963$
$a_{3,r} = 0.29724$,	$b_{3,r} = 0.54854$
$a_{4,r} = 0.05846$,	$b_{4,r} = 0.09098$
$a_{5,r} = -0.11558$,	$b_{5,r} = -0.09251$
$a_{0,r} = 0.45579$	
Angular interaction function	
$a_{1,\varphi} = -0.00610$,	$b_{1,\varphi} = 0.31622$
$a_{2,\varphi} = -0.35811$,	$b_{2,\varphi} = 0.29020$
$a_{3,\varphi} = -0.25341$,	$b_{3,\varphi} = -0.05585$
$a_{4,\varphi} = -0.13541$,	$b_{4,\varphi} = 0.00799$
$a_{5,\varphi} = -0.07183$,	$b_{5,\varphi} = 0.00425$
$a_{0,\varphi} = 0$	

oscillators, each cluster state persists over a range of roughly $0.25 \times (2\pi/\omega)$ of delay after it first occurs, as in Fig. 3. With relaxation oscillators, each cluster state persists over a range of roughly $0.125 \times (2\pi/\omega)$, as in Fig. 6(a). The relaxation oscillators tend to alternate between primary and secondary states as τ is varied. The primary states appear near multiples of $0.25 \times (2\pi/\omega)$ delay. As τ is ramped, the phase differences between subsequent elements might vary. As a consequence there could be different phase differences between subsequent elements. This gives rise to the secondary states that appear in between the primary states.

For examples of secondary states, Fig. 7 shows several experimental time series and corresponding schematic diagrams. Figure 7(a) depicts a *compressed splay state*. As in the splay state, we have $\varphi_4 - \varphi_3 = \varphi_3 - \varphi_2 = \varphi_2 - \varphi_1$, but these phase differences are different from a multiple of $\pi/2$ (marked by x in the schematic diagram). There also exists a *reverse compressed splay state* as shown in Fig. 7(b). Another secondary state is the *open two-cluster state* displayed in Fig. 7(c). For this state, the phase differences $\varphi_3 - \varphi_1$ and $\varphi_4 - \varphi_2$ are equal, but the two clusters have a phase lag between them.

As expected from the experiment [cf. Fig. 6(a)], the open two-cluster states are located between the two-cluster branch of solutions and the reverse splay branch in numerical studies [cf. Fig. 6(b)]. Likewise, the compressed reverse splay states are located between the reverse splay branch and the in-phase branch and the compressed splay states are located between the in-phase branch and the next splay branch (not shown).

The sequence of cluster states in Fig. 6 may seem somewhat arbitrary at first inspection. For example, when $\tau \approx 0.875 \times (2\pi/\omega)$ and the branch of compressed reverse splay states becomes unstable, why does the system transition to an in-phase state when a two-cluster state is also stable at this value of τ according to Fig. 6(b)? When we examine an example time series of the compressed reverse splay state in Fig. 7(b), we can see that the phase differences of this state are much closer to those of an in-phase state than to those of a two-cluster state. The experimental states observed depend upon both initial conditions and system parameters, as is typical for systems with multistability.

Having the set of primary states in mind, one might ask if there is also a scenario of a *compressed two-cluster state*, when $\varphi_1 = \varphi_3$ and $\varphi_2 = \varphi_4$, but the phase differences between the two clusters is no longer equal to π. Indeed, we find this state as shown in Fig. 7(d). The corresponding range of appropriate τ-values is illustrated in Fig. 8. This figure depicts an experimental measurement for a narrower τ-range and a starting configuration different from Fig. 6 (see black arrow) is implemented. This explains why the compressed two-cluster state was not found in Fig. 6 and thus reflects the multistability

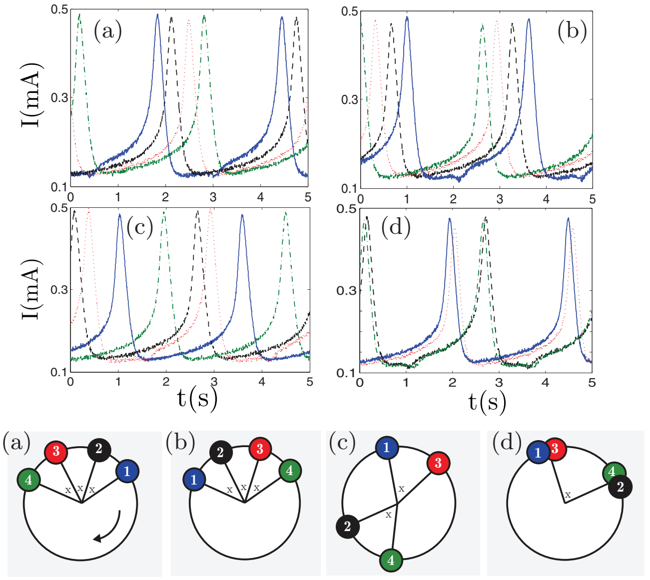

FIG. 7. (Color online) Experimental time series (top) and schematic diagram (bottom) for (a) a compressed splay state, (b) reverse compressed splay state, (c) open 2-cluster state, (d) compressed 2-cluster state. For the relaxation oscillators, these are in addition to the possible states seen in Fig. 3. Parameters: $V_0 = 1.2$ V, $K = 0.10$; time delays: (a) $\tau = 1.11 \times 2\pi/\omega$, (b) $0.82 \times 2\pi/\omega$, (c) $0.59 \times 2\pi/\omega$ with $\omega = 2.43$ rad/s as in Fig. 6 and (d) $0.68 \times 2\pi/\omega$ with $\omega = 2.492$ rad/s as in Fig. 8.

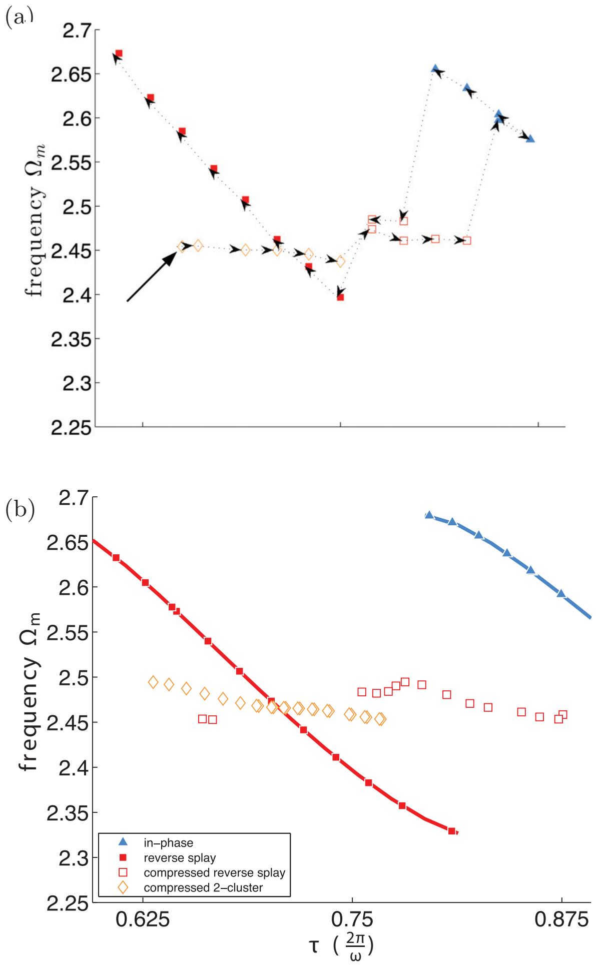

FIG. 8. (Color online) Frequency vs. time delay. (a) Experimental data, $V_0 = 1.2$ V, $K = 0.10$. The starting state is marked by a black arrow. The increasing and decreasing of τ during the experiment are shown with arrows. (b) Numerical results of Eqs. (16) using DDE-BIFTOOL (markers) and solutions of Eqs. (4) (lines). The interaction functions H_r and H_φ are chosen as in Eqs. (16) and Table I. Parameters: $\lambda = 2.890$, $K = 0.189$, and $\omega = 2.492$.

present in the system. Again, only numerical solutions relevant to the states found in the experiment are shown.

A. Extended theory

The experiments shown in the previous section for the relaxation oscillator motivate an extension of the theory introduced in Sec. II. The extended theory includes the interaction functions with a high order of Fourier coefficients and takes into account the existence of the secondary states. The secondary states can be obtained from Eqs. (16) with the Fourier coefficients given in Table I, if we assume nonequal radii and phase differences. With the ansatz $r_j = \text{const.} \equiv r_{0,j}$, and $\varphi_j = \Omega t + \Delta\varphi_j$, $\Delta\varphi_j \in \mathbb{R}$, Eqs. (16) yield

$$0 = \left(\lambda - r_{0,j}^2\right) r_{0,j} + K r_{0,j+1} c_r^j, \tag{17a}$$

$$\Omega = \omega - \gamma r_{0,j}^2 + K r_{0,j+1}/r_{0,j} c_\varphi^j, \tag{17b}$$

where we used the abbreviation

$$\begin{aligned} c_i^j \equiv \sum_{l=1}^{L} \{ & a_{l,i} \cos[l(\Delta\varphi_{j+1} - \Delta\varphi_j - \Omega\tau)] \\ & + b_{l,i} \sin[l(\Delta\varphi_{j+1} - \Delta\varphi_j - \Omega\tau)]\}. \end{aligned} \tag{18}$$

Equation (17) is an eight-dimensional ($\Delta\varphi_1 = 0$ without loss of generality) system of transcendental equations that can be solved numerically. The variational equation reads

$$\dot{\boldsymbol{\xi}}_j = \mathbf{J}_j \xi_j + \mathbf{R}_j \boldsymbol{\xi}_{j+1}(t - \tau), \tag{19}$$

with the matrices

$$\mathbf{J}_j = \begin{pmatrix} \lambda - 3r_{0,j}^2 & -K r_{0,j+1} d_r^j \\ -2\gamma r_{0,j} - K \frac{r_{0,j+1}}{r_{0,j}^2} c_\varphi & -K \frac{r_{0,j+1}}{r_{0,j}} d_\varphi^j \end{pmatrix}, \tag{20}$$

and

$$\mathbf{R}_j = K \begin{pmatrix} c_r^j & r_{0,j+1} d_r^j \\ c_\varphi^j / r_{0,j} & r_{0,j+1}/r_{0,j} d_\varphi^j \end{pmatrix}, \tag{21}$$

using the abbreviation

$$\begin{aligned} d_i^j \equiv \sum_{l=1}^{L} \{ & -a_{l,i} \sin[l(\Delta\varphi_{j+1} - \Delta\varphi_j - \Omega\tau)] \\ & + b_{l,i} \cos[l(\Delta\varphi_{j+1} - \Delta\varphi_j - \Omega\tau)]\}. \end{aligned} \tag{22}$$

Because of the unequal phase differences and radii, the variational equation cannot be block-diagonalized (cf. Sec. II) but the Floquet exponents Λ can be obtained from the transcendental equation $\det \mathbf{M} = 0$, where the matrix $\mathbf{M}$ has the following form:

$$\mathbf{M} = \begin{pmatrix} \mathbf{J}_1 - \Lambda \mathbf{I}_2 & \mathbf{R}_1 e^{-\Lambda\tau} & 0 & 0 \\ 0 & \mathbf{J}_2 - \Lambda \mathbf{I}_2 & \mathbf{R}_2 e^{-\Lambda\tau} & 0 \\ 0 & 0 & \mathbf{J}_3 - \Lambda \mathbf{I}_2 & \mathbf{R}_3 e^{-\Lambda\tau} \\ \mathbf{R}_4 e^{-\Lambda\tau} & 0 & 0 & \mathbf{J}_4 - \Lambda \mathbf{I}_2 \end{pmatrix}. \tag{23}$$

Solutions of Eq. (17) that were found to be stable ($\Lambda < 0$) are plotted as lines in Figs. 6(b) and 8(b). As expected, the lines perfectly agree with the points obtained by the analysis using DDE-BIFTOOL. The disadvantage of this analytic method compared to using the continuation software is that it is difficult to find all solutions of Eq. (17); i.e., in Figs. 6(b) and 8(b) the secondary states were not found analytically but only with the help of DDE-BIFTOOL. However, the analytic method gives further insight into the system, making analysis easier.

VII. DISCUSSION

We have applied a theoretical analysis of the delay-coupled Stuart-Landau model to a system of chemical oscillators. The results of experiment and theory match reasonably well for cluster synchronization with constant phase lag; the experiment also shows an additional type of dynamics with delay-dependent phase lag. For these secondary states the need for a more general approach arises, and we have extended the model to account for details in the coupling scheme. This approach allows us to approximate the experimental interaction functions and include them into the theoretical model. This yields numerical results that agree well with the experimental measurements in a parameter regime where the standard Stuart-Landau model is no longer appropriate.

This work is a good example for the interplay between theory and experiment, whereby the theory motivates the experiment and the experiment inspires the improvement or extension of the theory. On the one hand, the experiment presents an opportunity to apply the existing theory. The comparison of results for smooth oscillations shows that the theory accurately predicts the order of the cluster transitions in dependence upon the coupling delay and even predicts the frequencies of each state very well. On the other hand, we have found a difference in the stability of some states for smooth oscillators. The use of simple sine and cosine functions as interaction functions can no longer be justified, in particular for the radial interaction function. In experiments with relaxation oscillators, we observe additional secondary cluster states with different phase lags between subsequent clusters. By implementing an extended theory, we realize good agreement between theory and experiment. We can now explain with the theory the order of transitions between different cluster states first observed in the experiment. The range of stability of each solution branch matches to a large extent. There is still a difference between the exact frequencies of each state, but this is due to the drift in the intrinsic frequencies of the chemical oscillators in the experiment.

Our theoretical approach has been shown to produce good results for a system that is not necessarily located near the Hopf bifurcation. This means that the extended model, which accommodates for arbitrary interaction functions, is applicable to complex nonsinusoidal systems. Although we only consider unidirectional rings, it is interesting to note that the experimental apparatus allows large flexibility in the applied coupling topology.

ACKNOWLEDGMENTS

This work was supported by DFG in the framework of SFB 910, and in part by the National Science Foundation (CBET-0730597). P.H. acknowledges support by the Federal Ministry of Education and Research (BMBF), Germany (Grant No. 01GQ1001B).

[1] R. Albert and A.-L. Barabási, Rev. Mod. Phys. **74**, 47 (2002).

[2] A. S. Pikovsky, M. Rosenblum, and J. Kurths, *Synchronization: A Universal Concept in Nonlinear Sciences* (Cambridge University Press, Cambridge, 2003), Vol. 12.

[3] S. Boccaletti, V. Latora, Y. Moreno, M. Chavez, and D. U. Hwang, Phys. Rep. **424**, 175 (2006).

[4] *Handbook of Chaos Control*, edited by E. Schöll and H. G. Schuster, 2nd ed. (Wiley-VCH, Weinheim, 2008).

[5] E. Schöll, in *Advances in Analysis and Control of Time-Delayed Dynamical Systems*, edited by J.-Q. Sun and Q. Ding (World Scientific, Singapore, 2013), Chap. 4, pp. 57–83.

[6] D. Pazó, N. Montejo, and V. Pérez-Muñuzuri, Phys. Rev. E **63**, 066206 (2001).

[7] V. Dziubak, Y. L. Maistrenko, and E. Schöll, Phys. Rev. E **87**, 032907 (2013).

[8] F. Sorrentino and E. Ott, Phys. Rev. E **76**, 056114 (2007).

[9] T. Dahms, J. Lehnert, and E. Schöll, Phys. Rev. E **86**, 016202 (2012).

[10] P. S. Skardal, E. Ott, and J. G. Restrepo, Phys. Rev. E **84**, 036208 (2011).

[11] J. Kestler, W. Kinzel, and I. Kanter, Phys. Rev. E **76**, 035202 (2007).

[12] J. Kestler, E. Kopelowitz, I. Kanter, and W. Kinzel, Phys. Rev. E **77**, 046209 (2008).

[13] C. U. Choe, H. Jang, V. Flunkert, T. Dahms, P. Hövel, and E. Schöll, Dyn. Sys. **28**, 15 (2013).

[14] Y. Aviad, I. Reidler, M. Zigzag, M. Rosenbluh, and I. Kanter, Opt. Express **20**, 4352 (2012).

[15] R. Vardi, A. Wallach, E. Kopelowitz, M. Abeles, S. Marom, and I. Kanter, Europhys. Lett. **97**, 066002 (2012).

[16] M. R. Tinsley, S. Nkomo, and K. Showalter, Nature Phys. **8**, 662 (2012).

[17] C. R. S. Williams, T. E. Murphy, R. Roy, F. Sorrentino, T. Dahms, and E. Schöll, Phys. Rev. Lett. **110**, 064104 (2013).

[18] D. P. Rosin, D. Rontani, D. J. Gauthier, and E. Schöll, Phys. Rev. Lett. **110**, 104102 (2013).

[19] C. U. Choe, T. Dahms, P. Hövel, and E. Schöll, Phys. Rev. E **81**, 025205(R) (2010).

[20] C. U. Choe, T. Dahms, P. Hövel, and E. Schöll, in *Proceedings of the Eighth AIMS International Conference on Dynamical Systems, Differential Equations and Applications* (American Institute of Mathematical Sciences, Springfield, MO, USA, 2011), pp. 292–301, DCDS Supplement, Sept. 2011.

[21] L. M. Pecora and T. L. Carroll, Phys. Rev. Lett. **80**, 2109 (1998).

[22] D. Haim, O. Lev, L. M. Pismen, and M. Sheintuch, J. Phys. Chem. **96**, 2676 (1992).

[23] I. Z. Kiss, Y. Zhai, and J. L. Hudson, Ind. Eng. Chem. Res. **41**, 6363 (2002).

[24] C. G. Rusin, H. Kori, I. Z. Kiss, and J. L. Hudson, Phil. Trans. R. Soc. A **368**, 2189 (2010).

[25] I. Z. Kiss, Y. Zhai, and J. L. Hudson, Phys. Rev. Lett. **94**, 248301 (2005).

[26] K. Engelborghs, T. Luzyanina, and G. Samaey, K.U. Leuven Technical Report No. TW-330, http://www.cs.kuleuven.be/publicaties/rapporten/tw/TW330.abs.html.

[27] K. Engelborghs, T. Luzyanina, and D. Roose, ACM Trans. Math. Software **28**, 1 (2002).

[28] J. Miyazaki and S. Kinoshita, Phys. Rev. E **74**, 056209 (2006).

[29] I. Z. Kiss, C. G. Rusin, H. Kori, and J. L. Hudson, Science **316**, 1886 (2007).